Materials Advances

ROYAL SOCIETY OF CHEMISTRY

PAPER

View Article Online
View Journal | View Issue

Cite this: *Mater. Adv.*, 2025, **6**, 8586

Low-cost synthesis and comprehensive characterization of Cr^{3+} and Sn^{2+} co-doped lead sulfide thin films for optoelectronic applications

Athar Javed,*[a] Muhammad Abdul Wahab,[a] Muhammad Bashir,[b] Mashkoor Ahmad,[c] Syed Hussnain Haider Sherazi[a] and Shanza[a]

Received 20th August 2025,
Accepted 3rd October 2025

DOI: 10.1039/d5ma00934k

rsc.li/materials-advances

This study investigates the microstructural, compositional inhomogeneity and optoelectronic characteristics of Cr^{3+} and Sn^{2+} co-doped lead sulfide (PbS) films. X-ray diffraction reveals that all films are highly crystalline and possess a cubic structure. FTIR spectra show absorption peaks of Pb–S stretching with trace impurities like Pb–O, C–H and C–O–H. Raman spectra reveal vibrational modes of Pb–S with extra peaks and/or modes showing minor impurity content of PbO, $PbSO_4$, $Cr_2(SO_4)_3$ and SnO. All films exhibit uniform surface morphology. The Cr and Sn-doped PbS films possess different degrees of microstructural features and grain size distribution (in the range 120–325 nm). EDX analysis shows near-stoichiometric composition of Pb and S. EDX examination reveals that the Cr and Sn-doped PbS films exhibit 4.7 at% Cr and 4.3 at% Sn content, which is close to the intended (5.0 at%) doping level set during chemical synthesis. The un-doped PbS, 5% Cr-doped PbS and PbS film co-doped with 5% Cr + 5% Sn show hydrophobic surfaces unlike the substrate, whereas the 5% Sn-doped PbS film exhibits hydrophilic/hydrophobic borderline surface wettability character. The doping of Cr^{3+} and Sn^{2+} ions in PbS tunes the energy band gap, which is observed to be varied between 1.60 eV and 1.98 eV. Electrical measurements reveal the improved electrical characteristics of the Cr, Sn-doped films and among the investigated films, the 5% Sn-doped film possesses the lowest electrical resistivity (1.48 Ω cm). The experimental results show that the Cr, Sn-doped lead sulfide films possess a suitable combination of structural, chemical and physical properties suitable for optoelectronic applications.

1. Introduction

Metal-chalcogenides are an important class of semiconductor materials because of their suitable characteristics which include narrow band gap characteristics, high light absorption, high structural stability and environmentally friendly behavior.[1,2] Binary metal chalcogenides doped with suitable metal and/or transition metal elements have been studied for the purpose of band gap engineering and material design according to the application area.[3–9] However, tailoring the material's properties according to the requirements and fields of application, band gap engineering remains a great challenge for researchers, engineers and semiconductor industrialists to integrate semiconductor materials in optoelectronic devices.[10] Group IV–VI materials are of research interest due to their structural stability, tunable optoelectronic characteristics and environmentally friendly behavior.[11] IV–VI semiconductor materials have applications in infrared photography,[12] photovoltaic devices,[13] infrared detectors,[14] solar control coatings,[15] optoelectronics,[12] humidity and temperature sensors[13] and diode lasers.[16] The phase composition, structural stability, and optoelectronic properties of IV–VI compounds rely on the nature of the dopant (metal, transition metal and/or rare-earth element) because the nature of the dopant significantly alters the phase composition, chemical stability and morphological features.[3–8] In recent years, binary lead chalcogenides (such as PbS, PbSe, and PbTe),[17–22] zinc sulfide (ZnS),[23] tin sulfide (SnS)[24] and other group IV–VI compounds have been studied widely to explore their optoelectronic properties for applications in modern devices. PbS is a binary semiconductor compound that belongs to the IV–VI group.[25–28] Bulk PbS crystallizes in a cubic structure (space group: $Fm\bar{3}m$) and has a direct electronic energy band gap $E_g = 0.41$ eV.[26] In the PbS crystal structure, lead (Pb) atoms are located at atomic sites with coordinates (0,0,0), (1/2,1/2,0), (1/2,0,1/2) and (0,1/2,1/2), while sulfur (S) atoms

---

[a] Thin Film Laboratory, Department of Physics, University of the Punjab, Lahore-54590, Pakistan. E-mail: athar.physics@pu.edu.pk

[b] Microsystems Laboratory, Department of Physics and Applied Mathematics, Pakistan Institute of Engineering and Applied Sciences, Nilore, Islamabad-44000, Pakistan

[c] Nanomaterials Research Group, Physics Division, Pakistan Institute of Nuclear Science and Technology, Nilore, Islamabad-44000, Pakistan

attain atomic sites having coordinates (1/2,1/2,1/2), (0,0,1/2), (0,1/2,0) and (1/2,0,0), respectively. Under pressure (= 2.2 GPa), its rock-salt type cubic structure converts to an orthorhombic crystal structure, which further transforms to a cesium chloride (CsCl) type of crystal structure at a pressure of 21.2 GPa.[17]

Previous studies on thin films show that thin PbS films have E_g varying in the range of 0.43–2.2 eV depending on the method and deposition conditions of film preparation.[29–33] PbS in thin film form crystallizes in a face centered cubic (fcc) structure and exhibits a Bohr exciton radius equals to ∼18 nm.[25] The crystallite size being relatively equal in size to the Bohr exciton radius (∼18 nm) also shows the quantum confinement effect.[25] This paves the way for improvement in its physicochemical properties to meet desired applications in the field of optoelectronics.[25] Moreover, PbS film has shown better photoconductivity in the near-infrared (NIR) region as compared to other chalcogenides.[3] As described above, the E_g of chalcogenides can be varied largely through suitable doping of elements from the periodic table. So far, the effect of doping of Cd, Sn, Cr, Fe, Ca, Cu and Au on the chemical, structural, physical and optical characteristics of binary PbS films has been explored theoretically and experimentally by different research groups.[3–8] When PbS film is doped with metal ions of ionic radius less than the ionic radius of Pb (1.23 Å), the metal-doped PbS film exhibits a crystallite size that is found to decrease with increasing doping content.[3–8] The decreasing crystallite size influences the optical properties of the PbS films significantly.[3–8] Also, in most studies, the E_g of the doped-PbS films is observed to be larger than that of un-doped PbS films.[5,34–37] Tin (Sn) has an ionic radius of 1.22 Å, which is approximately equal to the Pb ionic radius (1.23 Å).[4] Studies on Sn-doped PbS films show an increase of crystallite size with increasing Sn concentration.[4,38] Whereas, the E_g is found to vary over a very narrow range (0.44 eV to 0.43 eV). The engineering of the E_g of binary PbS films through co-doping of suitable metal or transition metal elements is an alternate approach to enhance the material's performance from an applications point-of-view. So far, very limited studies exploring the effects of co-doping exist in the literature. For example, PbS films co-doped with Cd and Mn have been synthesized by the solvothermal microwave irradiation method.[39] PbS films co-doped with Bi, Cd and Er are also synthesized by chemical bath deposition (CBD) and characterized.[40] This study shows an increase of E_g significantly (0.5 eV to 2.3 eV) with an increase in the concentration of co-dopants.[40] Though separate reports exist exploring the role of Cr and/or Sn concentration on the optoelectronic properties of Cr-doped and Sn-doped PbS films,[5,41] according to our knowledge to-date, no study exists in the literature studying the effects of Cr and Sn co-doping in PbS films. In this study, the structural, phase composition, surface morphological, wettability characteristics and optoelectronic properties of binary PbS, 5% Cr-doped PbS, 5% Sn-doped PbS and (5% Cr + 5% Sn) co-doped PbS films are systematically investigated in-detail by employing experimental techniques.

2. Materials and methods

2.1 Cleaning of substrates

For film deposition, Corning glass slides (dimension: 75 mm × 25 mm × 2 mm) were used as the substrate. First, the glass slides were cleaned to remove surface contaminations and native oxides. The substrate cleaning was done by adopting a standard procedure and steps as described in ref. 42. In brief, the glass slides were washed/cleaned with detergent and running water. After cleaning with deionized water, the glass slides were placed in hot chromic acid (for 15 min) to remove native oxides. Ultrasonic cleaning of the substrates was carried-out in isopropyl alcohol and acetone. Finally, the air dried glass substrates were used for film deposition.[24]

2.2 Preparation of bath solution and film deposition

Pure (un-doped) PbS, 5% Cr-doped PbS, 5% Sn-doped PbS and (5% Cr + 5% Sn) co-doped PbS films are fabricated on clean glass substrates. Note, 5% doping of Cr and Sn in PbS is done by mol%. Bath solution of 100 ml volume was prepared by taking the appropriate amounts of lead acetate $[Pb(CH_3COO)_2]$, NaOH, thiourea $[SC(NH_2)_2]$ and dopant ion source. Lead acetate is a source of Pb^{2+} ions, while thiourea provides S^{2-} ions. NaOH is used to adjust the solution pH. It also acts as a complexing agent and reduces the concentration of free Pb^{2+} ions during chemical reactions.[43] For deposition of PbS film (un-doped), 3 ml (1 M) lead acetate $[Pb(CH_3COO)_2{\cdot}3H_2O]$, 3 ml (1 M) thiourea $[(H_2N)_2CS]$ and 6 ml (1 M) NaOH were added in deionized water to prepare a homogeneous 100 ml solution. The mixture solution was continuously magnetically stirred (for 2 to 4 min). NaOH was added as required to adjust the solution pH to 12. After preparing the solution, the cleaned substrates were immersed (which remain slightly inclined) in a glass beaker containing bath solution. The glass beaker covered with thin aluminum foil was kept in a laboratory oven (at 70 °C) and left for film deposition. After about 25 to 35 min, the substrates with deposition on were taken-out from the oven and washed with tap water and then dried in air.

During the chemical bath deposition process, the bath solution undergoes the following chemical reactions:[41]

$$Pb(CH_3COO)_2 + 2NaOH \rightarrow Pb(OH)_2 + 2Na(CH_3COO) \quad (1)$$

$$Pb(OH)_2 + 4NaOH \rightarrow Na_4Pb(OH)_6 \quad (2)$$

$$Na_4Pb(OH)_6 \rightarrow 4Na + HPbO_2^+ + 3OH^- + H_2O \quad (3)$$

$$SC(NH_2)_2 + OH^- \rightarrow CH_2N_2 + H_2O + SH^- \quad (4)$$

$$HPbO_2^+ + SH^- \rightarrow PbS + 2OH^- \quad (5)$$

The 5% Cr-doped PbS, 5% Sn-doped PbS and (5% Cr + 5% Sn) co-doped PbS films were deposited by following similar steps. Briefly, for deposition of the 5% Cr and 5% Sn-doped PbS films, appropriate amounts of the precursors of the dopants were added in 100 ml solution before adding thiourea. Note that the concentration of lead acetate was reduced accordingly. Table S1 summarizes the precursors and their quantities used in the preparation of a bath solution to deposit PbS, 5% Cr-doped

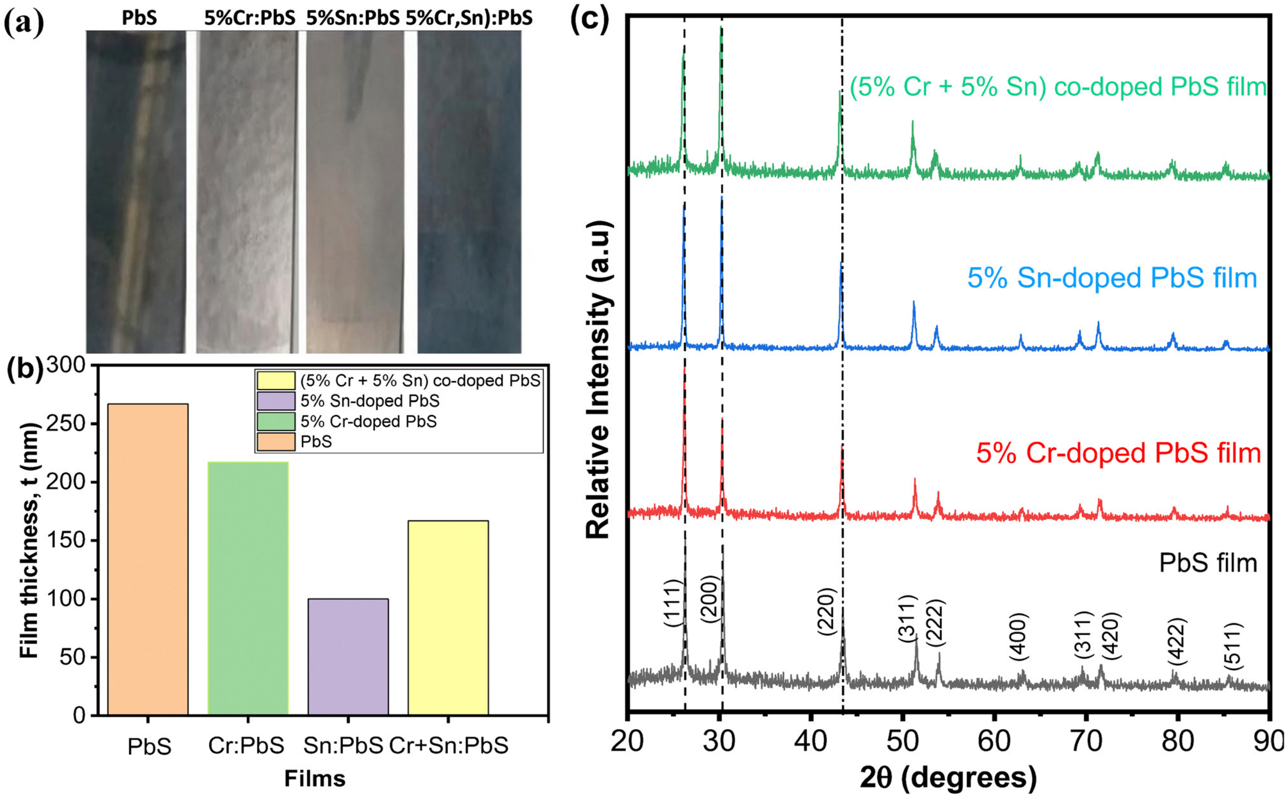

Fig. 1 (a) Photograph showing the physical appearance of Cr and Sn-doped PbS films, (b) variation of film thickness of Cr and Sn-doped PbS films and (c) X-ray diffractograms of Cr and Sn-doped PbS films.

PbS, 5% Sn-doped PbS and (5% Cr + 5% Sn) co-doped PbS films. After deposition of all films, it is noted that the appearance of the films is varied a little in their colors and the films are relatively smooth. Fig. 1a shows a photograph of the PbS film, 5% Cr-doped PbS film, 5% Sn-doped PbS film and (5% Cr + 5% Sn) co-doped film.

2.3 Characterization

An X-ray diffractometer (Model: Panalytical Empyream X'Pert[3] MRD) with a copper target (wavelength, λ = 1.5406 Å) was employed to investigate the crystal structure. To collect X-ray diffraction (XRD) data, the diffractometer was run (in θ–2θ geometry) by applying a tube voltage/current of 40 kV/35 mA. An FTIR spectrophotometer (Model: Nicolet™ iS50) was employed to collect FTIR spectra in the wave-number range of 400–4000 cm^{-1}. A Raman spectrometer (MST-4000A/Dong Woo Optron Co. Ltd) was used to collect the Raman spectra. The wettability test was performed by using a Tensiometer (Model: FTA200). The wettability test involves measuring the water-contact angle (WCA) at the film surface. Deionized (DI) water and diidomethane were taken as polar and non-polar (dispersive) liquids, respectively. For both liquid (DI water and diidomethane) droplets, an average sessile volume = 2.0 μl was taken. The surface free energy was calculated from the measured contact angles of both liquids (see details later in Section 3.4). A double beam UV-visible spectrophotometer (Model: U-2800) was employed for optical measurements. The absorbance spectra were collected by operating spectrophotometer with a scan rate of 2200 nm min^{-1}. Absorbance spectra were taken by setting a wavelength range (200 nm to 1000 nm) of interest.

A scanning electron microscope (Model: SEM/MAIA3 TESCAN) operated at 10.0 kV was used to examine the surface morphology. To examine electrical characteristics, the current–voltage characteristic curves of each film were traced by employing a Keithley 4200-SCS semiconductor characterization system. The resistivity ρ was determined using the equation $\rho = RA/L$, where R = sample resistance, which is equal to the inverse of the slope of the linear portion of the I–V data obeying Ohm's law, A represents the film area and L = the spacing between the two-probes.

The thickness (t) of each film was calculated by the gravimetric method as follows:[44]

$$t = \frac{m}{\rho A} \tag{6}$$

where m and A represent the mass and area of the film on the substrate, whereas ρ is the density of the material. The value of ρ taken for PbS was 7.6 g cm^{-3}.[45] For the PbS, 5% Cr-doped PbS, 5% Sn-doped PbS and (5% Cr + 5% Sn) co-doped PbS films, the film thickness was found to be 290 ± 3 nm, 217 ± 3 nm, 100 ± 2 nm and 167 ± 2 nm, respectively. With fixed deposition conditions and tight control over the CBD parameters (such as solution pH, deposition temperature and precursor concentration), a synthesis experiment was performed to confirm the reproducibility, adhesion and overall quality of the films. Each time the film's quality and adhesion is found to be better and the thickness is found to vary within the uncertainty of film thickness data. Fig. 1b shows the change in film thickness of the PbS, 5% Cr-doped PbS, 5% Sn-doped PbS and (5% Cr + 5% Sn) co-doped PbS film.

3. Results and discussion

3.1 Crystalline phase and structural properties

Fig. 1c displays the XRD scans of the binary PbS film, 5% Cr-doped PbS film, 5% Sn-doped PbS film and (5% Cr + 5% Sn) co-doped PbS thin film. XRD scans of all four films show good crystallinity and the films are polycrystalline in nature. Several sharp and high intensity diffraction peaks appear in the XRD scans (see Fig. 1c). In all films, the most intense peaks are observed to occur at $2\theta = 26.18^\circ$, 30.32°, 43.56°, 51.55° and 53.90° which occur due to diffraction from the (111), (200), (220), (311), and (222) atomic planes, respectively (Fig. 1c). The occurrence of sharp peaks indicates that all films possess polycrystalline nature and this is consistent with ref. 44. Furthermore, all peaks observed in the XRD scans (Fig. 1c) are found to match exactly with JCPDS card #05-0592.[44] However, with metal (Cr and Sn) doping in the PbS film, peak shifting towards smaller 2θ angles is observed, which is due to homogeneous strain occurring due to replacement of Pb ions by metal (Cr and/or Sn) ions in the host lattice.[4] It was expected because when chromium with a smaller ionic radius (0.069 nm) replaces Pb ions in the lattice, it causes strain due to the change in lattice parameters.[5] The analysis of the XRD data (Fig. 1c) confirms that all four films maintain the fcc structure.[44] Furthermore, no diffraction peaks related to impurities (metal sulfides or metal oxides) are observed in any film. A low content of metal oxide, metal sulfide and other trace impurities may be present (in chemically bath deposited films) along with the main cubic phase, which is impossible to detect in standard XRD measurements due to the detection limit of the X-ray diffractometer. For all films, the comparison of the relative intensities of all peaks shows slight variation of the crystallite growth orientation. For example, for the PbS film, the (111) peak is the highest intensity peak showing the preferred crystallite growth along the [111] crystallographic direction. For the 5% Cr-doped PbS film and 5% Sn-doped PbS film, the relative intensity of the highest intensity (111) and (200) peaks is found to be varied (with Cr and Sn doping) as compared to the un-doped PbS film. For the (5% Cr + 5% Sn) co-doped PbS film, the intensity of the (200) reflection is higher as compared to the (111) diffraction peak, which means that for the (5% Cr + 5% Sn) co-doped PbS film, the preferred growth direction of the crystallites is along the [200] direction instead of the [111] crystallographic direction.

To quantify and explain the variation of the preferred growth direction of the crystallites in the metal-doped PbS films, the texture coefficient (TC) for each film was calculated by using a method proposed by Harris as follows:[41,46]

$$\mathrm{TC}(hkl) = \frac{I^{\mathrm{m}}_{(hkl)} \Big/ I^{\mathrm{o}}_{(hkl)}}{\dfrac{1}{n}\sum I^{\mathrm{m}}_{(hkl)} \Big/ I^{\mathrm{o}}_{(hkl)}} \tag{7}$$

where $I^{\mathrm{m}}_{(hkl)}$ and $I^{\mathrm{o}}_{(hkl)}$ represent the measured and reference intensity of the crystallographic peaks, respectively, which are observed in Fig. 1c. Note that $I^{\mathrm{o}}_{(hkl)}$ is taken from the JCPDS card. n = number of diffraction peaks considered in the calculation of TC. A large value of TC of a specific (hkl) plane indicates the preferred texture of the film, indicating that more crystallites grow along that direction.[46] If TC = 1, then it shows that the crystallites are randomly oriented and do not have any preferred growth direction. If TC < 1 for the given (hkl) plane, then it indicates less random orientation of the crystallites. If TC > 1, then it indicates that the crystallites have a preferred growth direction along a certain [hkl] direction.[47] Calculation of TC data (Table 1) reveals that the crystallite growth changes from the [111] to [200] direction for the 5% Cr + 5% Sn co-doped PbS film. This variation in growth direction is possibly due to the ionic radii of the dopant ions ($r_{\mathrm{Cr}^{3+}}$ = 0.69 Å and $r_{\mathrm{Sn}^{2+}}$ = 1.18 Å) substituted in place of Pb ions ($r_{\mathrm{Pb}^{2+}}$ = 1.19 Å).[36]

To calculate the lattice constant, the spacing between the atomic planes (d_{hkl}) is calculated by using Bragg's diffraction condition as follows:[5]

$$d_{hkl} = \frac{\lambda}{2\sin\theta} \tag{8}$$

where λ = 1.5406 Å (the wavelength of Cu-K$_\alpha$ line), and d_{hkl} is the spacing between the atomic planes, while θ is a diffraction angle.[27,48]

Table 1 Calculated texture coefficient (TC) and lattice constant of the Cr, Sn-doped PbS films

Film	Peak	β (°)	β (radian)	2θ (°)	TC	d (Å)	a_{hkl} (Å)	a (Å)
PbS	(111)	0.26	0.004538	26.3	1.05	3.390	5.871	5.875 ± 0.004
	(200)	0.27	0.004712	30.4	0.84	2.940	5.880	
5% Cr:PbS	(111)	0.36	0.006283	26.2	0.91	3.400	5.889	5.891 ± 0.002
	(200)	0.38	0.006632	30.3	0.78	2.946	5.893	
5% Sn:PbS	(111)	0.25	0.004363	26.1	1.16	3.408	5.904	5.905 ± 0.001
	(200)	0.20	0.003491	30.2	0.97	2.953	5.906	
5% Cr + 5% Sn:PbS	(111)	0.38	0.006632	26.1	0.93	3.416	5.916	5.917 ± 0.001
	(200)	0.35	0.006109	30.2	0.97	2.959	5.918	

The lattice constant (a_{hkl}) of cubic films is determined by using the following relation:[5]

$$a_{hkl} = d_{hkl}\sqrt{(h^2 + k^2 + l^2)} \tag{9}$$

Using eqn (8) and (9), the calculated lattice constants are presented in Table 1. Compared with the PbS film, it is noted that the calculated value of a is increased with doping of Cr, Sn and (Cr + Sn) in the PbS film. For the PbS film, 5% Cr-doped PbS film, 5% Sn-doped PbS film and (5% Cr + 5% Sn) co-doped PbS film, the calculated average values of the lattice constants are 5.875 ± 0.004 Å, 5.891 ± 0.002 Å, 5.905 ± 0.001 Å and 5.917 ± 0.001 Å, respectively (Table 1). With doping of 5% Cr, 5% Sn and (5% Cr + 5% Sn) in the PbS film, the variation of the lattice constant (a) exhibits the trend as follows: $a_{\text{PbS film}} < a_{\text{5\%Cr-doped PbS film}} < a_{\text{5\%Sn-doped PbS film}} < a_{\text{(5\%Cr+5\%Sn)co-doped Pbs film}}$. The large value of cubic lattice constant of the 5% Cr-doped PbS film, 5% Sn-doped PbS film and (5% Cr + 5% Sn) co-doped PbS film as compared to the lattice constant of the PbS film indicates that the atoms of the metal dopant (Cr, Sn) replace lead (Pb) atoms in the $\text{Pb}_x\text{X}_{1-x}\text{S}$ system. With doping, an increase of lattice constant indicates the expansion of the unit cell and means that doping causes an increase in tensile strain.[5] For all films, the average value of crystallite size is also calculated by using the Scherrer relation as follows:[44]

$$D_{hkl} = \frac{k\lambda}{\beta\cos\theta} \tag{10}$$

where shape factor k = 0.89, β = full-width at half maxima and θ is a diffraction angle. Calculations reveal that the PbS film has a relatively large crystallite size (see Table 2). Doping of 5% Cr in PbS reduces the crystallite size significantly, whereas doping of 5%Sn in PbS increases the crystallite size (Table 2). The co-doping of (5% Cr + 5% Sn) in PbS results in a crystallite size closer to the value of D calculated for the 5% Cr-doped film (Table 2). In the case of the 5% Cr-doped PbS film, the average crystallite size decreased from 30 nm to 22 nm. This is consistent with the literature on Cr-doped PbS films.[5,41] For the 5% Sn-doped PbS film, the crystallite size increases with Sn-doping. This is also in accordance with the literature.[4] Thus, the doping of Cr and Sn (being different in ionic radii) when replacing Pb atoms in the PbS crystal structure results in different crystallite sizes.[4,41]

Table 2 Calculated crystallographic and microstructural parameters for the Cr/Sn-doped PbS films

Film	Plane	D_{hkl} (nm)	D_{ave} (nm)	ε ($\times10^{-3}$)	δ ($\times10^{15}$ m^{-2})
PbS	(111)	31	30 ± 1	1.12	0.90
	(200)	30			
5% Cr:PbS	(111)	22	22 ± 1	1.59	1.87
	(200)	21			
5% Sn:PbS	(111)	32	36 ± 4	0.96	0.65
	(200)	40			
5% Cr + 5% Sn:PbS	(111)	21	22 ± 1	1.55	1.79
	(200)	24			

Dislocation line density (δ), which determines the length of the dislocation lines/area, is also evaluated for all films. The estimation of δ gives a quantitative measure of the surface density of imperfections and defects present in the polycrystalline materials. For all films, the dislocation line density (δ) and inhomogeneous microstrain (ε) are also determined by a method proposed by Williamson and Smallman:[4]

$$\delta = \frac{1}{(D_{\text{ave}})^2} \tag{11}$$

$$\varepsilon = \frac{\beta\cos\theta}{4} \tag{12}$$

Table 2 presents the calculated values of δ and ε for the investigated metal-doped PbS films. From Table 2, it can be seen that the calculated δ and ε for the 5% Cr-doped PbS film, 5%Sn-doped PbS film and (5% Cr + 5% Sn) co-doped PbS film are different from those of the binary PbS film. The calculated values of δ reflect that the doping of different metals results in different degrees of defects and imperfections. The ionic radii of Cr^{3+}, Sn^{2+} and Pb^{2+} ions are 0.69 Å, 1.18 Å and 1.19 Å, respectively.[4,5] Higher dislocation density of the 5% Cr-doped PbS film indicates that the 5% Cr doping induces more defects, which could be due to the different ionic radii of Cr and Pb.[5] Low dislocation density in 5% Sn-doped PbS film suggests that the 5% Sn doping in PbS film results in less defects, which could be due to the similar ionic radii of Sn and Pb.[49] For the (Cr, Sn) co-doped film, the dislocation density is almost the same as that calculated for the 5% Cr-doped PbS film, which is due to the dominant effect of Cr-doping resulting in defects. For the PbS film, 5% Cr doped PbS film, 5% Sn doped PbS film and (5% Cr + 5% Sn) co-doped PbS film, the positive value of micro-strain (ε) indicates the occurrence of inhomogeneous tensile strain in all films. Among the investigated films, it has been noted that the 5% Cr-doping induces a higher degree of strain, while the 5% Sn-doped PbS films exhibit lower strain. The different degree of micro-strain in the metal-doped PbS films is associated with different ionic radii of Pb and the dopant element. Among the films, the 5% Cr-doped PbS film experiences larger strain, which is due to the different ionic radii of Cr^{3+} and Pb^{2+}. The least micro-strain is seen in the 5% Sn-doped PbS film, which is due to the similar ionic radii of Sn^{2+} and Pb^{2+}. This is consistent with the findings of Chalapathi *et al.*[4] The analysis and comparison of the calculated microstrain for the 5% Cr-doped PbS film and (5% Cr + 5% Sn) co-doped PbS film indicates that the 5% Cr-doping in PbS leads to more strain in the lattice due to the significantly different ionic radii of Cr^{3+} and Pb^{2+} because the ionic radii of the Sn^{2+} and Pb^{2+} ions are similar, thus causing a relatively lower strain.

3.2 FTIR and Raman analysis

Fig. S1 displays the FTIR spectra of the PbS, 5% Cr-doped PbS, 5% Sn-doped PbS and (5% Cr + 5% Sn) co-doped PbS films. The FTIR spectra confirm the appearance of absorption peaks related to the PbS phase in all films, along with peaks indicating the presence of different functional groups or impurities. Peaks in the wavenumber range of 460–480 cm^{-1} are related to Pb–S bond stretching and a similar peak corresponding to Pb–S bonds has been found in ref. 50 and 51. For the PbS film, prominent absorption peaks appear at 460 cm^{-1}, 749 cm^{-1}, 860 cm^{-1}, and 1381 cm^{-1} (Fig. S). The peak at 460 cm^{-1} indicates the PbS phase.[50] In the FTIR spectra, the peak appearing in the wave-number range 735–750 cm^{-1} shows the formation of lead oxide (PbO) and it has also been identified in PbS films studied by other research groups.[52,53] The peak that appeared around 860 cm^{-1} gives evidence of bond stretching related to C–H groups.[54] The peak in the wavenumber range 1370–1385 cm^{-1} corresponds to C–O–H (or CH_2) bond stretching.[55,56] For the 5% Cr-doped PbS thin film, promising absorption peaks appear at 465 cm^{-1}, 744 cm^{-1}, 859 cm^{-1}, and 1935 cm^{-1} (Fig. S1). The peak at 465 cm^{-1} is an indication of the PbS phase,[50] whereas the peaks at 744 cm^{-1} and 859 cm^{-1} show Pb–O and C–H bond stretching, respectively[52] and the band located at 1935 cm^{-1} is related to the C=O vibrational mode, which shows traces of carbonyl groups.[57] For the 5% Sn-doped PbS thin films, significant absorption peaks located at 456 cm^{-1}, 664 cm^{-1}, 1025 cm^{-1}, and 2350 cm^{-1} with minor peaks at 410 cm^{-1}, 436 cm^{-1} and 497 cm^{-1} are clearly observed (see Fig. S1). The low intensity peak at 436 cm^{-1} comes from the substrate due to the low thickness of the 5% Sn-doped PbS film and it is similar to ref. 58. The peak noticed at 456 cm^{-1} is related to the main PbS phase. The absorption peak at 664 cm^{-1} indicates the formation of tin-oxide (Sn–O) in the Sn-doped PbS film because in other studies on SnS and/or Sn-doped PbS films, this peak is observed at 650 cm^{-1} and identified as Sn–O bond stretching.[59,60]

The band around 1025 cm^{-1} is identified and marked to show C–N bond stretching vibrations.[58] The band present at 2350 cm^{-1} indicates atmospheric CO_2 that adsorbed on the film due to environmental exposure after deposition.[61] For the (5% Cr + 5% Sn) co-doped PbS thin film, the absorption bands are observed to be present at 475 cm^{-1}, 736 cm^{-1}, 849 cm^{-1}, 1639 cm^{-1}, and 1954 cm^{-1} with narrow bands at 431 cm^{-1}, and 635 cm^{-1} (Fig. S1). The peak present at 475 cm^{-1} is related to Pb–S bond stretching and represents a peak of the PbS main phase. The peaks present at 736 cm^{-1} and 849 cm^{-1} correspond to Pb–O and =C–H functional groups, respectively and are similar to peaks observed in the 5% Cr-doped PbS film. The peak at 1639 cm^{-1} is assigned to O–H bonding vibrations.[58] Furthermore, in some studies, the stretching peaks of the C–N bond are identified in the wave-number range of 1640–1690 cm^{-1}.[62] The peak at 1935 cm^{-1} appears due to asymmetric methyl stretching because the band at about 1952 cm^{-1} has been indicated and marked as an asymmetric methyl stretching peak according to ref. 63. For a (5% Cr + 5% Sn) co-doped PbS film, the prominent peaks are located at 475 cm^{-1}, 635 cm^{-1}, 736 cm^{-1}, 849 cm^{-1}, 1639 cm^{-1} and 1954 cm^{-1}. The peak at 475 cm^{-1} indicates PbS phase. The peak at 616 cm^{-1} is related to Sn–S bond stretching because the band at about 616 cm^{-1} is found to be the Sn–S characteristic band, which is possibly shifted to higher wavenumber (635 cm^{-1}) as a result of co-doping of 5% Cr + 5% Sn in PbS.[58] The peak at 736 cm^{-1} shows the metal oxide (PbO) phase. The peak in the region 860–880 cm^{-1} indicates the C–H bonding and the peak at 849 cm^{-1} appeared probably due to C–H bond stretching. The peak in the wavenumber region 1640–1690 cm^{-1} indicates C=N stretching. The peak marked at 1639 cm^{-1} occurs due to C=N bonding. The peak at 1954 cm^{-1} is likely to be associated with the vibrational mode of CO bond stretching. The peak identified at 2350 cm^{-1} indicates the presence of CO_2. Table S2 summarizes the identified FTIR peaks and corresponding vibrational modes in the PbS film, 5% Cr-doped PbS film, 5% Sn-doped PbS film and (5% Cr + 5% Sn) co-doped PbS film.

Fig. S2 shows the Raman spectra of the un-doped PbS film, 5% Cr-doped PbS film, 5% Sn-doped PbS film and (5% Cr + 5% Sn) co-doped PbS film. For consistency and comparison, the Raman data of each film are measured and presented covering the Raman shift range 0–1200 cm^{-1} where most of the Raman peaks are observed. For the PbS film, the Raman peaks at 133 cm^{-1}, 205 cm^{-1}, 429 cm^{-1}, 600 cm^{-1}, 825 cm^{-1} and 961 cm^{-1} are observed (Fig. S2). For the PbS film, a sharp Raman peak occurring at 133 cm^{-1} corresponds to the main PbS phase and represents active phonon modes. Note, the overlapping of the peaks of transverse optical (TO) and transverse acoustic (TA) phonon modes (if active) is also observed around 133 cm^{-1}.[64,65] A shoulder peak observed at 205 cm^{-1} corresponds to the LO phonon mode. The peak observed at about 429 cm^{-1} is due to the second overtone of the LO (2LO) phonon mode.[64,65] The peak that appeared at 600 cm^{-1} is assigned as the third overtone of the LO (3LO) phonon mode.[66] A metal oxide peak usually appears at 824 cm^{-1}. The peak at 825 cm^{-1} indicates the oxidation of the film and is related to PbO, whereas the peak around 970 cm^{-1} indicates the formation of lead sulphates ($PbSO_4$). Such peaks related to PbO and lead sulphates have also been observed in other studies.[66] Thus, in our films, a peak noticed at 961 cm^{-1} is assigned to lead sulphates. For the 5% Cr-doped PbS film, Raman peaks at 133 cm^{-1}, 189 cm^{-1}, 441 cm^{-1}, 581 cm^{-1}, 824 cm^{-1}, 970 cm^{-1} and 1087 cm^{-1} are observed (see Fig. S2). The peak at 133 cm^{-1} is a combination of TA and TO phonon modes and is a characteristic of the main PbS phase.[2] The peak at 189 cm^{-1} could be a combination of LO and TO modes.[67] The peak at 441 cm^{-1} is observed due to the second overtone (2LO) of the LO phonon mode.[2] The Raman peak at 581 cm^{-1} is attributed to the third overtone (3LO) of the LO phonon. This peak is similar to that seen at 600 cm^{-1} for the PbS film and it is shifted towards a higher Raman shift due to 5% Cr-doping in PbS. The presence of a peak at the Raman shift of 824 cm^{-1} indicates the formation of CrO.[68] The peak positioned at the Raman shift of 970 cm^{-1} might have appeared due to the amorphous phase of lead sulphates and/or lead oxide.[69] According to ref. 70, this peak could be a sign of $PbCr_{1-x}S_xO_4$ as a minor impurity phase. The presence of the peak at about 1087 cm^{-1} indicates the formation of chromium sulfide as an impurity phase.[70] For the 5% Sn-doped PbS film, the peak at 133 cm^{-1} corresponds to the main PbS phase. The peak located at 265 cm^{-1} is due to the 2TO phonon mode of PbS. The peak noted at 265 cm^{-1} is a signature of the PbO phase and a similar PbO peak at 263 cm^{-1} has been identified in ref. 71. Some studies mark this peak, which corresponds to minor/impurity traces of $PbSnS_2$ and this peak is expected to appear at about 256 cm^{-1}.[72] The peak observed at 426 cm^{-1} occurred due to the second order overtone (2LO) of the LO phonon mode as reported in ref. 66. Whereas, the peak positioned at 963 cm^{-1} shows the presence of lead sulphate or tin sulphate.[66] For the (5% Cr + 5% Sn) co-doped PbS film, Raman peaks appear at 135, 196, 429, 602, 966 and 1106 cm^{-1} (see Fig. S2). The peak positioned at 135 cm^{-1} indicates the main PbS phase, while a peak positioned at 196 cm^{-1} appears due to the surface phonon mode and a similar peak related to the surface phonon mode has been reported in ref. 65. The peaks noticed at 135 cm^{-1}, 429 cm^{-1}, 602 cm^{-1} and 966 cm^{-1} in all films have already been discussed above. However, the additional peak at 1106 cm^{-1} indicates the S–O stretching mode.[73]

3.3 Elemental composition and surface morphology

EDX analysis of the PbS film, 5% Cr-doped PbS film, 5% Sn-doped PbS film, and (5% Cr + 5% Sn) co-doped PbS film was also performed in order to examine the element composition in the obtained films. Fig. S3 displays the EDX spectra of the PbS film, 5% Cr-doped PbS film, 5% Sn-doped PbS film, and (5% Cr + 5% Sn) co-doped PbS film. In the EDX spectra of all the films (Fig. S3), Pb and S are found as the main elements along with minor content of other elements as an impurity. For example, in the PbS film, the silicon (Si) peak as expected comes from the glass substrate. In the 5% Cr-doped PbS film, the Cr peak is detected, which indicates and confirms the addition of Cr in PbS. Similarly, the Sn peak in the 5% Sn-doped PbS film shows the presence of Sn in PbS. In the (5% Cr + 5% Sn) co-doped PbS film, the Cr and Sn peaks are obvious along with the main Pb and S peaks. Thus, the EDX spectrum of the PbS film co-doped with 5% Cr + 5% Sn (Fig. S3) confirms the successful co-doping of Cr and Sn in the PbS film. However, minor concentrations of some impurity elements (such as Si, Ca, Mg, Si and Na) are also detected in all films. These peaks mainly come from the glass substrate and are also observed in ref. 74. Similar EDX analysis results identifying the elemental composition in PbS and metal-doped PbS films are reported in ref. 4 and 5. Furthermore, the presence of a peak related to oxygen (O) indicates the oxidation of the films. The surface of the films can be oxidized due to exposure to the environment. Also, a trace of oxygen can come from the glass substrate or from precursors used during the chemical synthesis of the films. Quantitative analysis of the EDX data gives the elemental composition (in at%) of each element.

Table 3 presents the elemental composition of each film quantified in atomic percentage (at%). Analysis of the EDX data shows that after doping of 5% Cr in PbS, the achieved Cr content in the deposited film is 4.7 at% Cr (see Table 3), whereas the doping of 5% Sn in PbS gives a concentration of about 4.3 at% Sn. For the (5% Cr + 5% Sn) co-doped PbS film, 3.3 at% Sn and 3.7 at% Cr are found by EDX. EDX analysis confirms the successful doping of Cr and Sn in PbS and the elemental composition of the doped element is close to the actual concentration of the dopant as expected. However, some elements as minor impurities are also detected along with the main (Pb, S, Cr, Sn) elements (Table 3).

Table 3 Elemental composition (in at%) of the Cr and Sn-doped PbS films obtained by EDX analysis

	Obtained atomic percent of elements						
Film	Pb	S	Cr	Sn	C	O	Na
PbS	48.2	40.8	—	—	6.7	3.2	1.1
5% Cr:PbS	42.6	41.4	4.7	—	5.0	5.3	1.0
5% Sn:PbS	44.1	40.7	—	4.3	6.2	3.0	1.7
5% Cr + 5% Sn:PbS	36.3	43.0	3.7	3.9	6.8	4.4	1.9

Fig. 2 depicts the SEM micrographs of the PbS, 5% Cr doped PbS, 5% Sn doped PbS, (5% Cr + 5% Sn) co-doped PbS film. The polycrystalline nature of all films can be seen from the surface SEM micrographs (Fig. 2). The polycrystalline character of the films is consistent with the XRD results discussed above, which also show the polycrystalline structure of all films. Grains of pyramidal shape are observed from Fig. 2(a)–(d) for the PbS and metal-doped PbS films. The formation of pyramidal shaped grains has been reported for chemically synthesized PbS films and our findings of surface morphological features are consistent with ref. 41. Furthermore, analysis and comparison of the SEM images indicate that all films have different grain size with clear grain boundaries (Fig. 2a–d). Furthermore, PbS and metal-doped PbS films have a dense microstructure showing film deposition free from cracks and voids. The comparison of the micrographs (in Fig. 2a–d) clearly shows that the doping of different metal elements (Cr, Sn) in PbS results in different microstructural features. The white blobs seen in the SEM images (Fig. 2b and d) are also analyzed by EDX and are identified as a cluster of lead-rich PbS in Cr-doped PbS films. Probably, the cluster formation occurs due to inhomogeneity during the chemical synthesis or deposition process.[5]

Furthermore, the doping of different metal elements can alter the rate of chemical reaction, which can affect the homogeneity of the final solution used to deposit metal-doped PbS films. In CBD grown films, the dopant can alter the growth process and ultimately the nucleation of the depositing species due to a different rate of precipitation occurring during the film deposition.[40] By analyzing the SEM micrographs, the average grain sizes of all films are also calculated using imageJ software. Histograms showing the grain size distribution in all films are shown Fig. 2e–h. Histograms plots (Fig. 2e–h) provide in-depth insights to see the effects of doping elements on the grain size distribution. From Gaussian fitting to grain size distribution data, the average grain size of each metal-doped PbS film is also determined with uncertainty. It is noted that the PbS film has a grain size of 219 ± 94 nm. For the 5% Cr-doped PbS, the average grain size reduces and it is found to be 120 ± 45 nm. For 5% Sn-doped PbS, the average grain size is quite large and its estimated value is 325 ± 133 nm, whereas for (5% Cr + 5% Sn) co-doped PbS, the grain size is 150 ± 40 nm.

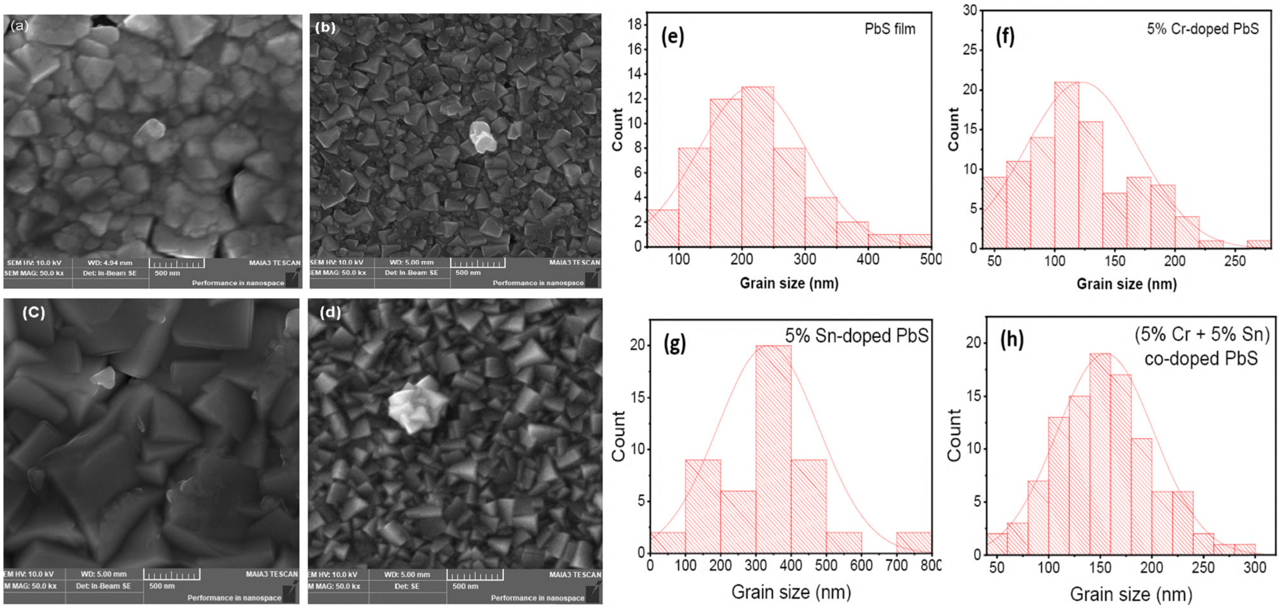

Fig. 2 SEM micrographs of the (a) PbS film, (b) 5% Cr-doped PbS film, (c) 5% Sn-doped PbS film, (d) (5% Cr + 5% Sn) co-doped PbS film, and (e)–(h) histograms showing the variation of the grain size in the Cr and Sn-doped PbS films.

3.4 Wettability behavior

In thin solid films, the stability of the film's surface depends on the film-substrate and film-air interface. In metallic and semiconductor films, the passivation, environmental exposure, surface roughness, composition and anti-aging properties alter the film's wetting characteristics.[75,76] Thus, the hydrophilic or hydrophobic nature of the films is also investigated by performing the wettability test on all films. Surface wetting behavior is studied by measuring the contact angles of a non-polar (dispersive) liquid (diidomethane) and a polar liquid (water) because both these liquids have known values of surface tension. Diidomethane is used because its surface tension is relatively higher than the surface tension of many other organic liquids and it helps to form a droplet shape and contact angle at most solid surfaces. Basically, a mathematical model employed for surface energy calculation requires two probe liquids with known values of surface tension and contact angle. Diidomethane facilitates determining the dispersive component of total surface energy. According to the Owens–Wendt model,[77] the surface energy ($\gamma_\mathrm{s} = \gamma_\mathrm{s}^\mathrm{p} + \gamma_\mathrm{s}^\mathrm{d}$) of a thin solid film is determined by solving the following equation for $\gamma_\mathrm{s}^\mathrm{p}$ and $\gamma_\mathrm{s}^\mathrm{d}$:[77,78]

$$(1+\cos\theta)\gamma_\mathrm{L} = 2\sqrt{\gamma_\mathrm{s}^\mathrm{d}\gamma_\mathrm{L}^\mathrm{d}} + 2\sqrt{\gamma_\mathrm{s}^\mathrm{p}\gamma_\mathrm{L}^\mathrm{p}} \tag{13}$$

where γ_L, $\gamma_\mathrm{L}^\mathrm{p}$ and $\gamma_\mathrm{L}^\mathrm{d}$ represent the surface tension, and polar and dispersive components of the liquids, respectively. The surface energy is calculated by solving the above equation for two values of contact angle of the two probe liquids (water and diidomethane).[78] For water (polar liquid), the values of γ_L, $\gamma_\mathrm{L}^\mathrm{p}$ and $\gamma_\mathrm{L}^\mathrm{d}$ are taken as 72.8, 51.0 and 21.8 mJ m^{-2}, respectively; whereas for the nonpolar (dispersive) liquid, the values of γ_L, $\gamma_\mathrm{L}^\mathrm{p}$ and $\gamma_\mathrm{L}^\mathrm{d}$ are taken as 50.8, 2.3 and 48.5 mJ m^{-2}, respectively.[79]

Photographs of de-ionized (DI) water drops forming contact angles (CAs) at the surface of PbS, 5% Cr-doped PbS, 5% Sn-doped PbS and (5% Cr + 5% Sn) co-doped PbS films are displayed in Fig. 3a–d. Table 4 summarizes the water contact angle (WCA) and surface free energy measured at the surface of the un-doped PbS, 5% Cr-doped PbS, 5% Sn-doped PbS and co-doped with 5% Cr + 5% Sn PbS films. All films (except 5% Sn:PbS film) represent hydrophobic surfaces having water contact angle ≥90°. A 5% Sn:PbS film exhibits hydrophobic/hydrophilic boarder-line wetting behavior because its WCA = 89° (see Fig. 3 and Table 4). Similar wettability behavior of metal doped films has been reported in ref. 80. However, the un-coated substrate shows a hydrophilic behavior with the lowest contact angle (CA) of 48°. A wettability test reveals that the PbS film deposited with 5% Cr-doping has the highest value of CA (119°). Thus, a 5% Cr-doped PbS film exhibits the highest degree of hydrophobicity. Semiconductor films with hydrophobic character are applicable for anti-corrosion coatings and self-cleaning surfaces. Hydrophobic semiconductor films with a suitable combination of optical properties when integrated in optical devices have the additional advantage of protecting the film from degradation and improving optical device stability.[75]

Fig. 3e presents the variation of the CAs and surface free energy of the un-doped PbS, 5% Cr-doped PbS, 5% Sn-doped PbS and PbS co-doped with 5% Cr + 5% Sn film. With 5% Cr doping in PbS, the DI water contact angle of the 5% Cr-doped PbS film is increased as compared to the PbS film. For the 5% Sn-doped PbS film, the water contact angle is decreased when compared with the 5% Cr-doped PbS film and even lower as compared to the contact angle of the PbS film. For the co-doped PbS film with 5% Cr + 5% Sn, the contact angle is increased but lower than that of the 5% Cr-doped PbS and un-doped PbS film. Whereas, the surface free energy is increased to its maximum

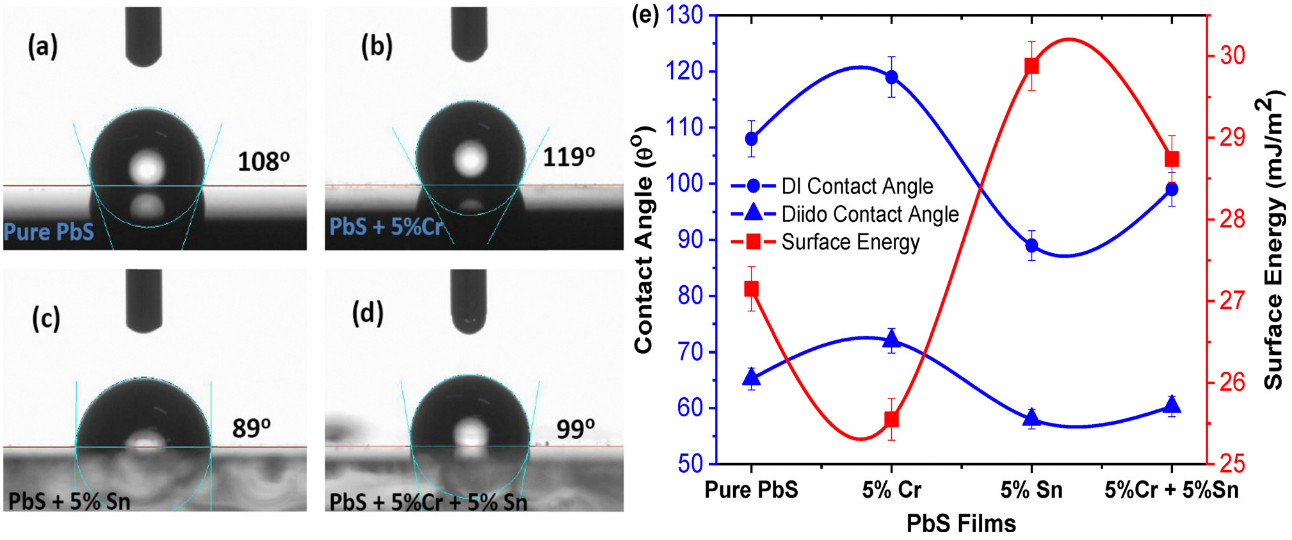

Fig. 3 Demonstration of DI water contact angles on the surface of the (a) PbS film, (b) 5% Cr-doped PbS film, (c) 5% Sn-doped PbS film and (d) 5% Cr + 5% Sn co-doped PbS film, and (e) the variation of the water contact angle and surface energy in the Cr, Sn-doped PbS films.

Table 4 Contact angles (CAs) and surface free energy of the 5% Cr and 5% Sn-doped PbS films

	Average contact angles (°)				
Film	DI water	Diidomethane	Dispersive (mJ m^{-2})	Polar (mJ m^{-2})	Surface energy (mJ m^{-2})
Glass substrate	48	65	17.65	33.18	50.83
PbS	108	65	26.97	0.19	27.15
5% Cr:PbS	119	72	24.17	1.38	25.55
5% Sn:PbS	89	58	28.29	1.59	29.88
5%Cr + 5%Sn:PbS	99	60	28.67	0.08	28.74

value (29.88 mJ m^{-2}) for the 5% Sn-doped PbS film. This increase in the surface energy is attributed to variation in the film's homogeneity and the chemical composition of the polar bonds between different molecular species. Furthermore, the change in surface free energy could be associated with the variation in surface morphology (grain size, grain boundaries and surface roughness).[80,81]

3.5 Optical characteristics

In order to elucidate the optical properties of the PbS film, 5% Cr-doped PbS film, 5% Sn-doped PbS and (5% Cr + 5% Sn) co-doped PbS film, optical measurements (absorbance and transmittance) were also carried-out by using a UV-visible spectrophotometer. Fig. 4a and b show the absorbance (*A*) and transmittance (*T*) behavior of the PbS film, 5% Cr-doped PbS film, 5% Sn-doped PbS and (5% Cr + 5% Sn) co-doped PbS film. For all films, the absorbance shows a decreasing trend with increasing wavelength (Fig. 4a). This kind of decreasing absorbance trend has also been observed in studies reported in ref. 7 and 82. Furthermore, the comparison of the absorbance spectra (in Fig. 4a) shows that the PbS film exhibits the lowest absorbance as compared to 5% Cr, 5% Sn and (5% Cr + 5% Sn) co-doped films. The absorbance plots of the PbS film and 5% Sn-doped PbS film show low intensity excitonic peaks in the range of 350–450 nm. These peaks are expected in polycrystalline semiconductors. These peaks are expected in thin films or in nanomaterials where the particle size is ≤18 nm or at least comparable with the Bohr radius.[83] The absorbance spectra of the PbS film doped with 5% Cr and co-doped with 5% Cr + 5% Sn show clear excitonic peaks in the wavelength range of 400–550 nm. Furthermore, it is noted that PbS films doped with 5% Cr, 5% Sn and 5% Cr + 5% Sn show an increase of absorbance as compared to the PbS film (Fig. 4a). This is consistent with earlier reports, which also show that the doping of different metals and/or transition metals in the PbS film enhances the absorbance of light as compared to un-doped PbS films.[3–8,83]

The transmittance behavior of the doped PbS films demonstrates that the doping of 5% Cr, 5% Sn and (5% Cr + 5% Sn) results in the decrease of %*T* (Fig. 4b). The decrease of %*T* in the 5% Cr, 5% Sn or 5% Cr + 5% Sn doped PbS film is due to the increase in light scattering losses.[84] However, for all films, %*T* is observed to be low (in visible region) and it increases with increase of the wavelength (Fig. 4b). As the analysis of the phase composition by FTIR and Raman spectroscopy described above show the formation of metal oxides and/or minor traces of other impurities along with the main PbS phase, the doping of Cr, Sn and Cr + Sn creates different degrees of crystal defects. These defects in the host PbS crystal lattice serve as scattering centers, causing the incident light to disperse resulting in a decrease of %*T*.[85]

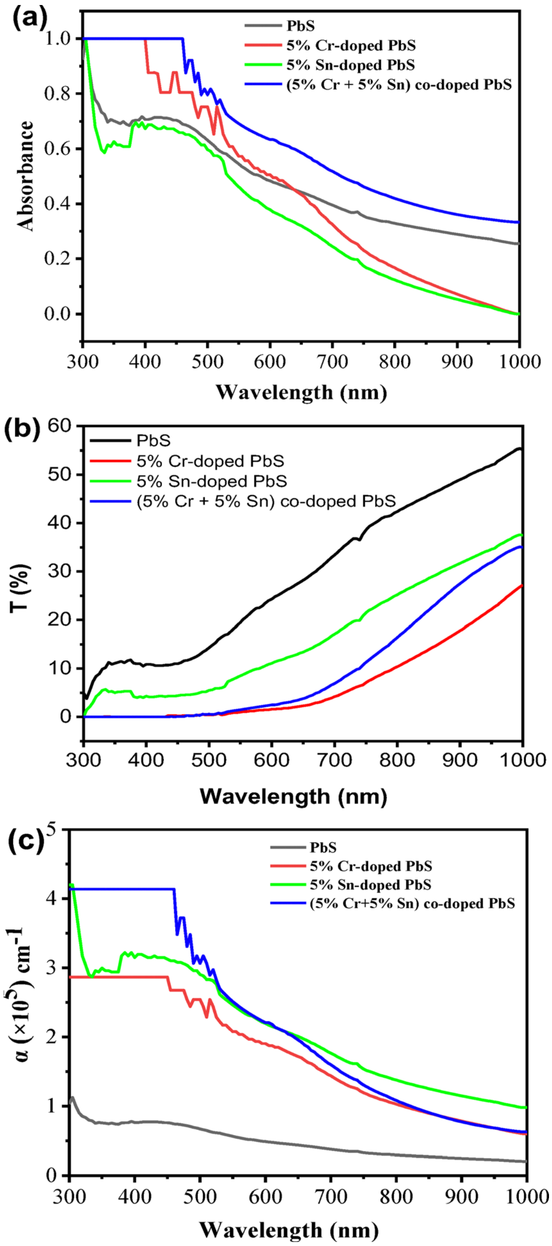

Fig. 4 Plots of (a) absorbance, (b) transmittance and (c) absorption coefficient for Cr and Sn-doped PbS films.

Using absorbance (A) data, the coefficient of optical absorption (α) is also calculated using the following relation:[86]

$$\alpha = \frac{2.303A}{t} \tag{14}$$

where t is the film thickness and A denotes absorbance.

Fig. 4c demonstrates the absorption coefficient variation with incident wavelength. For all films, the absorption coefficient (α) tends to decrease with increasing wavelength and all four films have $\alpha > 10^5$ cm^{-1} over the range of wavelength. The doping of 5% Cr and 5% Sn results in an increase of α and follows a similar decreasing trend with wavelength. Comparing the absorption coefficient plots of all four films (Fig. 4c), it is noticed that the PbS film exhibits a low absorption coefficient as compared to the Cr and Sn-doped PbS films. Among the films, the PbS film co-doped with 5% Cr + 5% Sn exhibits a higher value of α in the visible region. Thus, a significant increase in α is observed for the (5% Cr + 5% Sn) co-doped PbS film suitable for most optoelectronic devices to improve device performance and efficiency.

To investigate the transition behavior of an electron from the valence to the conduction band and the nature of the band gap (direct or indirect), the electronic energy band gap E_g is determined by the Tauc method.[55] For each film, the E_g is determined from the $(\alpha h\nu)^2$ *versus* energy ($h\nu$) plot according to the following equation:[55]

$$(\alpha h\nu)^n = B(h\nu - E_g) \tag{15}$$

where $n = 2$ (direct transition).

Fig. 5 depicts the Tauc plots of the PbS film, 5% Cr-doped PbS film, 5% Sn-doped PbS and (5% Cr + 5% Sn) co-doped PbS film. The energy band gap E_g is estimated from the linear fit to the data as shown in Fig. 5. The PbS film exhibits E_g = 1.98 eV. With doping of 5% Cr in PbS, the E_g of the 5% Cr-doped PbS film is decreased to E_g = 1.60 eV. With doping of 5% Sn in PbS, the E_g of the 5% Sn-doped PbS film is increased to E_g = 1.90 eV.

The PbS film co-doped with (5% Cr + 5% Sn) exhibits E_g = 1.64 eV (Fig. 5). Comparison of the Tauc plots (in Fig. 5) and E_g (in Fig. S4) indicates that the doping of metal elements (Cr, Sn) in PbS has a significant effect on E_g. For the films investigated here (PbS film and Cr, Sn-doped PbS films), the E_g is found to be varied in the range of 1.98 eV and 1.60 eV (Fig. S4). The wavelength corresponding to this range of E_g lies in the visible part of the electromagnetic spectrum. For the thin film photovoltaic device, the E_g of the absorber film should ideally match with the solar spectrum. Taking into account thermalisation and transparency losses, the E_g should lie in the range of 1.1–1.5 eV to achieve maximum device efficiency.[87] Among the films studied here, the 5% Cr-doped PbS film is a suitable material for thin film photovoltaic applications because its E_g matches with the solar spectrum.[88] Comparing the E_g of the PbS film with Cr, Sn-doped films, the change in E_g could be due to the Moss–Burstein effect causing red-shift in the optical E_g with doping.[34] The Moss–Burstein effect demonstrates that the metal (Cr^{3+}, Sn^{2+}) ion doping induces additional electron states in CB causing a decrease of E_g as compared to the binary PbS film. During electron transition from VB to CB, the filling of energy states in the CB causes a change in ΔE in the E_g of a semiconductor material.[34] Also, the red-shift might occur due to structural variation because of dopant ion (Cr^{3+}, Sn^{2+}) addition in place of Pb ions.[89] The optical properties (absorption coefficient and E_g) of the Cr and Sn-doped PbS films demonstrate that the PbS film and metal (Cr, Sn)-doped PbS films could be suitable materials for optoelectronic devices such as thin film photovoltaic applications, IR and visible photodetectors and gas sensors.

3.6 Electrical properties

The electrical behavior of the PbS, 5% Cr-doped PbS, 5% Sn-doped PbS and (5% Cr + 5% Sn) co-doped PbS films was also

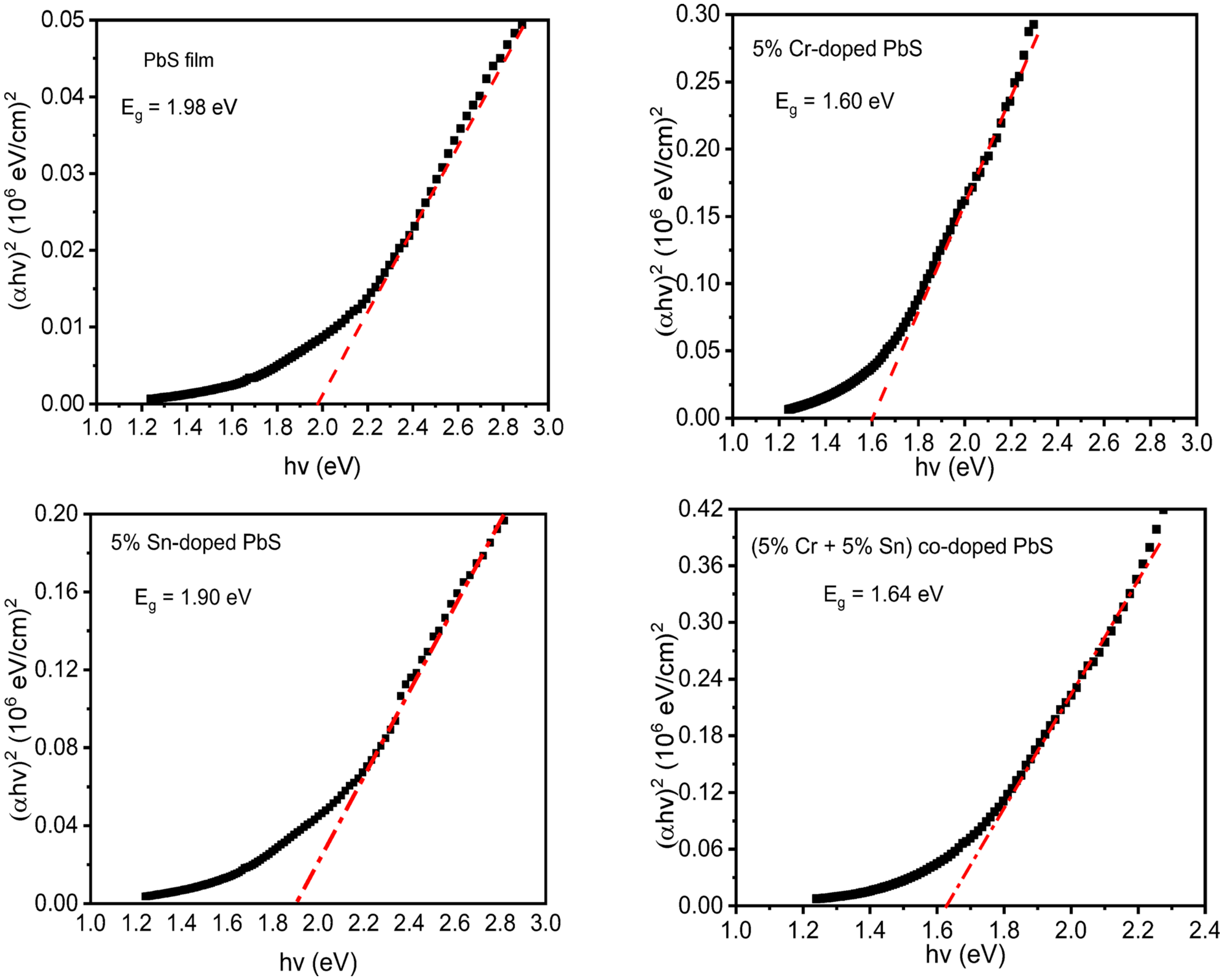

Fig. 5 Tauc plots of the Cr and Sn-doped PbS films.

studied by measuring the current–voltage characteristic curves. Fig. 6 displays the current–voltage characteristic curve of the PbS, 5% Cr-doped PbS, 5% Sn-doped PbS and (5% Cr + 5% Sn) co-doped PbS film. For a sweep voltage −25 V to +25 V, the characteristic curve of the PbS film and co-doped (with 5% Cr + 5% Sn) PbS film indicates almost similar behavior over this voltage range. These two films show semiconducting behavior in the range of ±15 V. Under similar bias conditions (in the sweep voltage range −15 V to +15 V), an increasing slope of the *I–V* characteristic curve of the 5% Cr-doped PbS film indicates a relatively better current flow (Fig. 6). This film shows semiconductor behavior between ±10 V. Whereas the 5% Sn-doped PbS film shows semiconductor behavior for low sweep voltage range ($\leq \pm 2.5$ V). For $V > \pm 2.5$ V, the 5% Sn-doped PbS film exhibits metallic nature because the *I–V* data meets the Ohmic behavior conditions and thus films behave like a resistor. From the *I–V* characteristic curve of each film (Fig. 6), the electrical resistivity (ρ) of each film is determined (as described in Section 2.3) by taking the slope of the linear part of the *I–V* data.

For the investigated films in this study, the calculated values of resistivity ρ are presented and compared with the literature in Table 5. Comparison of the *I–V* curves (in Fig. 6) and resistivity data (in Table 5) shows that the 5% Cr-doping in the PbS host lattice causes a decrease in ρ as compared to the

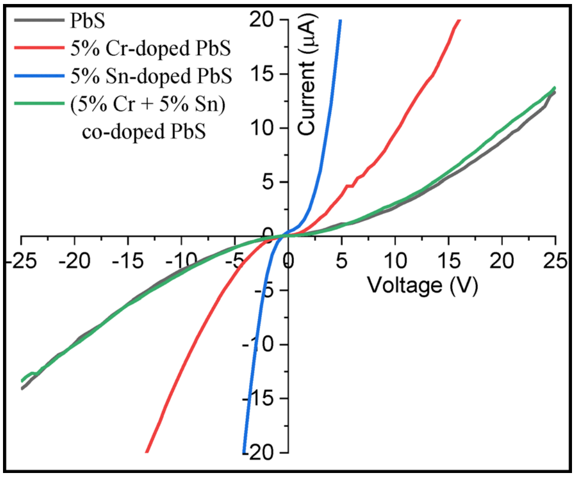

Fig. 6 *I–V* characteristic curves of the Cr and Sn-doped PbS films.

Table 5 Electrical resistivity (ρ) of the films calculated from the I–V data

Film	Deposition method	ρ (Ω cm)	Ref.
PbS	CBD	141	This work
PbS	CBD	16	90
5% Cr:PbS	CBD	34.62	This work
5% Cr:PbS	CBD	1.32	91
5% Sn:PbS	CBD	1.48	This work
3% Sn:PbS	CBD	1.49	4
5% Sn + 5% Cr:PbS	CBD	60.83	This work

un-doped PbS film. This is because, on Cr-doping, the Cr atoms replace Pb atoms in the PbS lattice and each Cr atom adds one more electron to the host (PbS) crystalline solid due to the difference in oxidation states of Cr and Pb ions.[92] As a result, an increasing number of electrons contributing to the flow of electrical current causes a decrease in resistivity. Similarly, due to the difference in oxidation states of Sn and Pb, the replacement of Pb by an Sn atom in the PbS lattice contributes two additional electrons per Sn atom, causing a significant decrease of ρ due to the increase in electron number density. For the PbS film co-doped with 5% Cr + 5% Sn, the ρ is increased (as compared to 5% Cr-doped and 5% Sn-doped PbS films) and its value is found to be 60.83 Ω cm (Table 5). This significant increase in ρ of the (Cr, Sn) co-doped film is due to the variation in crystallite size and chemical inhomogeneity.[91,92] The resistivity of semiconductor films (even films of the same material and composition when compared with films deposited by a similar route as in Table 5) can differ because of the difference in (i) crystallite size, (ii) degree of film oxidation and/or (iii) degree of formation of secondary phases. The resistivity is higher, if the crystallite size is lower and *vice versa*. Because due to small crystallite size, the carrier scattering by grain boundaries is large and thus, a smaller mean free path occurs, which results in higher resistivity.[93] Furthermore, the resistivity values of the PbS and 5% Cr:PbS films are found to be higher as compared to their values reported in ref. 90 and 91. This is because of different use of the precursors in the deposition of films by CBD. In most studies, the difference in electrical and optical properties is seen to arise due to different use of precursors and starting materials in the deposition of films.[4,90,91] For example, in ref. 4, the lead nitrate [$Pb(NO_3)_2$] is used as the Pb source; whereas in the present study, the lead acetate [$Pb(CH_3COO)_2{\cdot}3H_2O$] is used as a Pb source. In chemically bath deposited films, the use of different precursors leaves different effects on film properties due to different degrees of phase formation, secondary phases, impurities and inhomogeneity (such as seen in the comparison of this study and ref. 4). For the 5% Sn:PbS film (this study), the resistivity value matches with 3% Sn:PbS film studied in ref. 4 because of negligible impurities or inhomogeneity due to the low composition of Sn. Furthermore, in ref. 4, the doping effect of tin (Sn) up to 3% only is studied and no variation in band gap value occurred due to the low doping concentration. According to ref. 4, the calculated band gap values of PbS and 3% Sn doped PbS are quite low (0.43–0.44 eV). A 5%Sn:PbS film (this work) exhibits a band gap of 1.90 eV, which is quite large and an improved value as compared to ref. 4. The resistivity values are higher when compared to the resistivity values of our films of similar composition with ref. 90 and 91 deposited with a similar method. This difference in resistivity values could be due to the difference in crystallite size, grain boundaries, lattice defects and imperfections, because carrier scattering and thus mean free path is largely affected by grain boundaries. Less carrier scattering occurs, which leads to a decrease in resistivity if the crystallite size is large and *vice versa*. The combination of experimental results presented above indicates that among the investigated films, the 5% Sn:PbS film possesses a suitable combination of optical properties with the lowest ρ = 1.48 Ω cm and structural stability for optoelectronic applications.

4. Conclusions

In conclusion, the microstructural and compositional analysis, surface wetting (hydrophobic/hydrophilic) character and optoelectronic properties of un-doped PbS, 5% Cr-doped PbS, 5% Sn-doped PbS and (5% Cr + 5% Sn) co-doped PbS films are investigated experimentally. All films are polycrystalline and retain their cubic structure on Cr and Sn doping like the un-doped PbS film. No peaks of impurities/secondary phases are detected from the XRD spectra. The FTIR spectra show stretching peaks of Pb and S bonds with a signature of impurity peaks, indicating the formation of Pb–O, C–H and C–O–H bonds. The Raman spectra show peaks of PbS phase with some impurity peaks. A uniform surface morphology with different grain size distributions is seen from the SEM micrographs. EDX analysis shows composition of Pb and S near-stoichiometry. The surfaces of the doped films are hydrophobic with water contact angle $\geq 90^\circ$ except for the 5% Sn-doped PbS film. The PbS films doped with 5% Cr, 5% Sn and (5% Cr + 5% Sn) show high optical absorption coefficient. With 5% Cr and 5% Sn doping in PbS, the band gap varies in the range of 1.60 eV to 1.98 eV. Among the films, the 5% Sn-doped PbS film exhibits low resistivity (1.48 Ω cm). The combination of optical and electrical properties with structural stability shows the promising characteristics of the Cr, Sn-doped lead sulfide films for optoelectronic devices.

Author contributions

A. J.: conceptualization, resources, writing – original draft, project administration, funding acquisition, supervision. M. A. W.: conceptualization, investigation, formal analysis, visualization, writing – review & editing. M. B.: formal analysis, investigation, visualization, validation, writing – review & editing. M. A.: formal analysis, investigation, validation. S. H. H. S.: conceptualization, formal analysis. Shanza: investigation, formal analysis, visualization, validation.

Conflicts of interest

There are no conflicts to declare.

Data availability

All data and supporting information of this experimental study are available within this article and its supplementary information (SI). Supplementary information is available. See DOI: https://doi.org/10.1039/d5ma00934k.

Acknowledgements

Financial support by University of the Punjab through Project Grant No. D/1924/ORIC (2024–2025) is gratefully acknowledged.

References

1 F. G. Hone, F. K. Ampong, R. K. Nkum and F. Boakye, Band gap engineering in lead sulphur selenide ($PbS_{1-x}Se_x$) thin films synthesized by chemical bath deposition method, *J. Mater. Sci.: Mater. Electron.*, 2017, **28**, 2893–2900.

2 F. Gode, O. Baglayan and E. Guneri, P-type nanostructure PbS thin films prepared by the SILAR method, *Chalcogenide Lett.*, 2015, **12**, 519–528.

3 S. Thangavel, S. Ganesan, S. Chandramohan, P. Sudhagar, Y. S. Kang and C.-H. Hong, Band gap engineering in PbS nanostructured thin films from near-infrared down to visible range by in situ Cd-doping, *J. Alloys Compd.*, 2010, **495**, 234–237.

4 U. Chalapathi, S.-H. Park and W. J. Choi, Chemically deposited Sn-doped PbS thin films for infrared photodetector applications, *Appl. Phys. A*, 2021, **127**, 645.

5 A. M. Ahmed, M. Rabia and M. Shaban, The structure and photoelectrochemical activity of Cr-doped PbS thin films grown by chemical bath deposition, *RSC Adv.*, 2020, **10**, 14458–14470.

6 M. Shkir, B. Palanivel, K. V. Chandekar, A. Khan, A. M. El-Toni, A. A. Ansari, R. A. Zargar, M. Sayed and S. AlFaify, Microwave-assisted synthesis of Cu doped PbS nanostructures with enhanced dielectric and electrical properties for optoelectronic applications, *Mater. Sci. Eng., B*, 2021, **271**, 115268.

7 E. Yücel and Y. Yücel, Effect of doping concentration on the structural, morphological and optical properties of Ca-doped PbS thin films grown by CBD, *Optik*, 2017, **142**, 82–89.

8 N. Andrade Neto, Y. Oliveira, C. Paskocimas, M. Bomio and F. Motta, Increase of antimicrobial and photocatalytic properties of silver-doped PbS obtained by sonochemical method, *J. Mater. Sci.: Mater. Electron.*, 2018, **29**, 19052–19062.

9 P. Priyadarshini, S. Das and R. Naik, A review on metal-doped chalcogenide films and their effect on various optoelectronic properties for different applications, *RSC Adv.*, 2022, **12**, 9599–9620.

10 J. Piprek, *Semiconductor Optoelectronic Devices: Introduction to Physics and Simulation*, Elseiver Science, 2003.

11 C. Kamal, A. Chakrabarti and M. Ezawa, Direct band gaps in group IV–VI monolayer materials: Binary counterparts of phosphorene, *Phys. Rev. B*, 2016, **93**, 125428.

12 P. J. McCann, IV–VI Semiconductors for Mid-infrared Optoelectronic Devices, in *Mid-infrared Semiconductor Optoelectronics*, ed. A. Krier, Springer Series in Optical Sciences, Springer, London, 2006, vol. 118, pp. 237–264, DOI: 10.1007/1-84628-209-8_7.

13 H. Zogg, Photovoltaic IV–VI on silicon infrared devices for thermal imaging applications, Proc. SPIE 3629, Photodectors: Materials and Devices IV, (7 April 1999), DOI: 10.1117/12.344567.

14 P. J. McCann and Y. Selivanov, IV–VI Semiconductor Mid-IR Lasers, *MRS Proc.*, 2005, **891**, 0891-EE01-05, DOI: 10.1557/PROC-0891-EE01-05.

15 F.-J. Fan, L. Wu and S.-H. Yu, Energetic I–III–VI2 and I2–II–IV–VI4 nanocrystals: synthesis, photovoltaic and thermoelectric applications, *Energy Environ. Sci.*, 2014, **7**, 190–208.

16 H. Preier, Physics and applications of IV–VI compound semiconductor lasers, *Semicond. Sci. Technol.*, 1990, **5**, S12.

17 T. Chattopadhyay, H. Von Schnering, W. Grosshans and W. Holzapfel, High pressure X-ray diffraction study on the structural phase transitions in PbS, PbSe and PbTe with synchrotron radiation, *Phys. B + C*, 1986, **139–140**, 356–360.

18 M. Lach-Hab, D. A. Papaconstantopoulos and M. J. Mehl, Electronic structure calculations of lead chalcogenides PbS, PbSe, PbTe, *J. Phys. Chem. Solids*, 2002, **63**, 833–841.

19 J. N. Zemel, J. D. Jensen and R. B. Schoolar, Electrical and optical properties of epitaxial films of PbS, PbSe, PbTe, and SnTe, *Phys. Rev.*, 1965, **140**, A330.

20 Y.-L. Pei and Y. Liu, Electrical and thermal transport properties of Pb-based chalcogenides: PbTe, PbSe, and PbS, *J. Alloys Compd.*, 2012, **514**, 40–44.

21 J. Sun, Y. Zhang, Y. Fan, X. Tang and G. Tan, Strategies for boosting thermoelectric performance of PbSe: A review, *Chem. Eng. J.*, 2022, **431**, 133699.

22 Y. Xiao and L.-D. Zhao, Charge and phonon transport in PbTe-based thermoelectric materials, *npj Quantum Mater.*, 2018, **3**, 55.

23 A. Goswami and A. P. Goswami, Dielectric and optical properties of ZnS films, *Thin Solid Films*, 1973, **16**, 175–185.

24 P. Nair, A. Garcia-Angelmo and M. Nair, Cubic and orthorhombic SnS thin-film absorbers for tin sulfide solar cells, *Phys. Status Solidi A*, 2016, **213**, 170–177.

25 E. Pentia, L. Pintilie, I. Matei, T. Botila and E. Ozbay, Chemically prepared nanocrystalline PbS thin films, *J. Optoelectron. Adv. Mater.*, 2001, **3**, 525–530.

26 S. B. Qadri, A. Singh and M. Yousuf, Structural stability of PbS films as a function of temperature, *Thin Solid Films*, 2003, **431**, 506–510.

27 S. Sadovnikov and A. Gusev, Structure and properties of PbS films, *J. Alloys Compd.*, 2013, **573**, 65–75.

28 S. Sadovnikov, N. Kozhevnikova and A. Rempel, The structure and optical properties of nanocrytalline lead sulfide films, *Semiconductors*, 2010, **44**, 1349–1356.

29 D. H. Yeon, S. M. Lee, Y. H. Jo, J. Moon and Y. S. Cho, Origin of the enhanced photovoltaic characteristics of PbS thin film solar cells processed at near room temperature, *J. Mater. Chem. A*, 2014, **2**, 20112–20117.

30 B. Ezekoye, T. Emeakaroha, V. Ezekoye, K. Ighodalo and P. Offor, Optical and structural properties of lead sulphide (PbS) thin films synthesized by chemical method, *Int. J. Phys. Sci.*, 2015, **10**, 385–390.

31 A. Fouda, M. Marzook, H. Abd El-Khalek, S. Ahmed, E. Eid and A. El Basaty, Structural and optical characterization of chemically deposited PbS thin films, *Silicon*, 2017, **9**, 809–816.

32 P. Vidhya, K. Shanmugasundaram, P. Thirunavukkarasu, T. Govindaraj, V. Balasubramani, B. Yogeswari and M. Karuppusamy, Enhancement of optoelectronic properties of PbS thin films grown by Jet nebulizer spray pyrolysis technique for photodetector applications: an impact of substrate temperature, *J. Mater. Sci.: Mater. Electron.*, 2023, **34**, 1023.

33 D. Vankhade and T. K. Chaudhuri, Effect of thickness on structural and optical properties of spin-coated nanocrystalline PbS thin films, *Opt. Mater.*, 2019, **98**, 109491.

34 B. Touati, A. Gassoumi, I. Dobryden, M. M. Natile, A. Vomiero and N. K. Turki, Engineering of electronic and optical properties of PbS thin films via Cu doping, *Superlattices Microstruct.*, 2016, **97**, 519–528.

35 M. Ibrahim, M. Zayed, A. M. Ahmed, M. A. Ghanem, M. Shaban, S. Abd Elkhalik and F. Mohamed, Synthesis and characterization of Mo-doped PbS thin films for enhancing the photocatalytic hydrogen production, *Mater. Chem. Phys.*, 2024, **315**, 128962.

36 S. Ravishankar, A. Balu, K. Usharani, S. Balamurugan, D. Prabha and V. Nagarethinam, Optical and magnetic properties of PbS thin films doped with Fe^{2+} ions, *Optik*, 2017, **134**, 121–127.

37 B. Touati, A. Gassoumi, S. Alfaify and N. Kamoun-Turki, Optical, morphological and electrical studies of Zn: PbS thin films, *Mater. Sci. Semicond. Process.*, 2015, **34**, 82–87.

38 F. G. Hone, F. Dejene and O. Echendu, Band gap tailoring of chemically synthesized lead sulfide thin films by in situ Sn doping, *Surf. Interface Anal.*, 2018, **50**, 648–656.

39 R. S. S. Saravanan, M. Meena, D. Pukazhselvan and C. Mahadevan, Structural, optical and electrical characterization of Mn^{2+} and Cd^{2+} doped/co-doped PbS nanocrystals, *J. Alloys Compd.*, 2015, **627**, 69–77.

40 M. C. Portillo, O. P. Moreno, R. G. Pérez, R. P. Merino, H. S. Juarez, S. T. Cuapa and E. R. Rosas, Characterization and growth of doped-PbS in situ with Bi^{3+}, Cd^{2+} and Er^{3+} ions by chemical bath, *Mater. Sci. Semiconductor Process.*, 2017, **72**, 22–31.

41 J. Huo, W. Li and T. Wang, Effect of Cr doping concentration on the structural, optical, and electrical properties of lead sulfide (PbS) nanofilms, *Coatings*, 2019, **9**, 376.

42 A. Javed, Qurat-ul-Ain and M. Bashir, Controlled growth, structure and optical properties of Fe-doped cubic π-SnS thin films, *J. Alloys Compd.*, 2018, **759**, 14–21.

43 V. Şimşek and M. O. Çağlayan, Nanocrystalline PbS thin film produced by alkaline chemical bath deposition: effect of inhibitor levels and temperature on the physicochemical properties, *Int. J. Mater. Res.*, 2023, **114**, 1047–1057.

44 L. Beddek, M. Messaoudi, N. Attaf, M. Aida and J. Bougdira, Sulfide precursor concentration and lead source effect on PbS thin films properties, *J. Alloys Compd.*, 2016, **666**, 327–333.

45 R. Das and R. Kumar, Preparation of nanocrystalline PbS thin films and effect of Sn doping and annealing on their structural and optical properties, *Mater. Res. Bull.*, 2012, **47**, 239–246.

46 G. B. Harris, Quantitative measurement of preferred orientation in rolled uranium bars, *London, Edinburgh Dublin Philos. Mag. J. Sci.*, 1952, **43**, 113–123.

47 M. Kumar, A. Kumar and A. Abhyankar, Influence of texture coefficient on surface morphology and sensing properties of W-doped nanocrystalline tin oxide thin films, *ACS Appl. Mater. Interfaces*, 2015, **7**, 3571–3580.

48 J. Epp, *X-ray diffraction (XRD) techniques for materials characterization, Materials characterization using nondestructive evaluation (NDE) methods*, Elsevier, 2016, pp. 81–124.

49 W. D. Callister Jr. and D. G. Rethwisch, *Materials Science and Engineering: An Introduction*, John Wiley & Sons, 10th edn, 2020.

50 S. Rajathi, K. Kirubavathi and K. Selvaraju, Structural, morphological, optical, and photoluminescence properties of nanocrystalline PbS thin films grown by chemical bath deposition, *Arabian J. Chem.*, 2017, **10**, 1167–1174.

51 S. K. Pasha, K. Chidambaram, N. Vijayan and W. Madhuri, Structural and electrical properties of nano structure lead oxide, *Optoelectron. Adv. Mater., Rapid Commun.*, 2012, **6**, 110–116.

52 J. D. Patel, F. Mighri, A. Ajji and T. K. Chaudhuri, Morphology and size control of lead sulphide nanoparticles produced using methanolic lead acetate trihydrate-thiourea complex via different precipitation techniques, *Mater. Chem. Phys.*, 2012, **132**, 747–755.

53 S. Chen and W. Liu, Oleic acid capped PbS nanoparticles: synthesis, characterization and tribological properties, *Mater. Chem. Phys.*, 2006, **98**, 183–189.

54 J. Senvaitiene, J. Smirnova, A. Beganskiene and A. Kareiva, XRD and FTIR Characterisation of lead oxide-based pigments and glazes, *Acta Chim. Slov.*, 2007, **54**, 185–193.

55 A. Parveen, S. Agrawal and A. Azam, Band gap tuning and fluorescence properties of lead sulfide $Pb_{0.9}A_{0.1}S$ (A: Fe, Co, and Ni) nanoparticles by transition metal doping, *Opt. Mater.*, 2018, **76**, 21–27.

56 E. A. Disalvo, A. M. Bouchet and M. Frias, Connected and isolated CH_2 populations in acyl chains and its relation to pockets of confined water in lipid membranes as observed by FTIR spectrometry, *Biochim. Biophys. Acta*, 2013, **1828**, 1683–1689, DOI: **10.1016/j.bbamem.2013.02.007**.

57 F. G. Hone and F. B. Dejene, Chemosynthesis of nanostructures lead sulphide thin films from triethylamin (Et_3N) complexing agent, *Inorg. Chem. Commun.*, 2020, **111**, 107583.

58 M. Dar, D. Govindarajan and G. Dar, Comparing the electrochemical performance of bare SnS and Cr-doped SnS nanoparticles synthesized through solvothermal method, *Phys. Solid State*, 2021, **63**, 1343–1350.

59 J.-H. Zhao, R.-Q. Tan, Y. Yang, W. Xu, J. Li, W.-F. Shen, G.-Q. Wu, X.-F. Yang and W.-J. Song, Synthesis mechanism of heterovalent Sn_2O_3 nanosheets in oxidation annealing process, *Chin. Phys. B*, 2015, **24**, 070505.

60 L. Wang, D. Wang, Z. Dong, F. Zhang and J. Jin, Interface chemistry engineering of protein-directed SnO_2 nanocrystal-based anode for lithium-ion batteries with improved performance, *Small*, 2014, **10**, 998–1007.

61 S. G. Warren, W. J. Wiscombe and J. F. Firestone, Spectral albedo and emissivity of CO_2 in Martian polar caps: Model results, *J. Geophys. Res.: Solid Earth*, 1990, **95**, 14717–14741.

62 C. Preti, G. Tosi and P. Zannini, Investigations of chromium(III), manganese(III), tin(II) and lead(II) dithiocarbamate complexes, *J. Mol. Struct.*, 1980, **65**, 283–292.

63 C. Piliego, L. Protesescu, S. Z. Bisri, M. V. Kovalenko and M. A. Loi, 5.2% efficient PbS nanocrystal Schottky solar cells, *Energy Environ. Sci.*, 2013, **6**, 3054–3059.

64 T. D. Krauss, F. W. Wise and D. B. Tanner, Observation of coupled vibrational modes of a semiconductor nanocrystal, *Phys. Rev. Lett.*, 1996, **76**, 1376.

65 T. D. Krauss and F. W. Wise, Raman-scattering study of exciton-phonon coupling in PbS nanocrystals, *Phys. Rev. B: Condens. Matter Mater. Phys.*, 1997, **55**, 9860.

66 K. Nanda, S. Sahu, R. Soni and S. Tripathy, Raman spectroscopy of PbS nanocrystalline semiconductors, *Phys. Rev. B: Condens. Matter Mater. Phys.*, 1998, **58**, 15405.

67 Y. Bencherif, A. Boukra, A. Zaoui and M. Ferhat, Lattice dynamics study of lead chalcogenides, *Infrared Phys. Technol.*, 2011, **54**, 39–43.

68 R. Wilkins, The Raman spectrum of crocoite, *Mineral. Mag.*, 1971, **38**, 249–250.

69 B. Abdallah, R. Hussein, N. Al-Kafri and W. Zetoun, PbS thin films prepared by chemical bath deposition: effects of concentration on the morphology, structure and optical properties, *Iran. J. Sci. Technol., Trans. A: Sci.*, 2019, **43**, 1371–1380.

70 L. Monico, K. Janssens, E. Hendriks, B. G. Brunetti and C. Miliani, Raman study of different crystalline forms of $PbCrO_4$ and $PbCr_{1-x}S_xO_4$ solid solutions for the noninvasive identification of chrome yellows in paintings: a focus on works by Vincent van Gogh, *J. Raman Spectrosc.*, 2014, **45**, 1034–1045.

71 N. Mathews, C. Ángeles–Chávez, M. Cortés-Jácome and J. T. Antonio, Physical properties of pulse electrodeposited lead sulfide thin films, *Electrochim. Acta*, 2013, **99**, 76–84.

72 A. Łapińska, A. Taube, M. Wąsik, G. Z. Żukowska, A. Duzynska, J. Judek and M. Zdrojek, Raman spectroscopy of layered lead tin disulfide ($PbSnS_2$) thin films, *J. Raman Spectrosc.*, 2017, **48**, 479–484.

73 D. Manara, A. Grandjean, O. Pinet, J. Dussossoy and D. Neuville, Sulfur behavior in silicate glasses and melts: implications for sulfate incorporation in nuclear waste glasses as a function of alkali cation and V_2O_5 content, *J. Non-Cryst. Solids*, 2007, **353**, 12–23.

74 G. Bakiyaraj and R. Dhanasekaran, Synthesis and characterization of flower-like ZnSe nanostructured thin films by chemical bath deposition (CBD) method, *Appl. Nanosci.*, 2013, **3**, 125–131.

75 A. E. Bangera and K. Appaiah, Tunable wettability and prediction of total surface energy for nanocoatings: An empirical model, *Surf. Coating Technol.*, 2020, **383**, 125277.

76 Y. Luo, L. Ou, J. Chen, G. Zhang, Y. Xia, B. Zhu and H. Zhou, Understanding the wettability and natural floatability of PbS with different types of vacancy defects: A perspective from spin-polarized DFT-D and MD, *J. Mol. Liq.*, 2022, **359**, 119245.

77 D. K. Owens and R. C. Wendt, Estimation of the surface free energy of polymers, *J. Appl. Polym. Sci.*, 1969, **13**, 1741–1747.

78 M. Bashir and S. Bashir, Hydrophobic-hydrophilic character of hexamethyldisiloxane films polymerized by atmospheric pressure plasma jet, *Plasma Chem. Plasma Process.*, 2015, **35**, 739–755.

79 M. Żenkiewicz, Wettability and surface free energy of corona-treated biaxially-oriented polypropylene film, *J. Adhes. Sci. Technol.*, 2001, **15**, 1769–1785.

80 S. Hussnain, H. Sherazi, M. Bashir, M. Waqas Saleem, A. Javed, M. Ahmad and M. Abdul Wahab, Facile synthesis, microstructural, phase composition, wettability behavior and optical properties of Cu:PbS films for optoelectronic applications, *Mater. Chem. Phys.*, 2025, **338**, 130683.

81 J. Kaur, A. Khanna and A. K. Chawla, Metallic to semiconducting transition and hydrophobicity properties of indium films, *Vacuum*, 2022, **203**, 111281.

82 S. Thirumavalavan, K. Mani and S. Suresh, Investigation on structural, optical, morphological and electrical properties of lead sulphide (PbS) thin films, *J. Ovonic Res.*, 2015, **11**, 123–130.

83 N. P. Dasgupta, W. Lee and F. B. Prinz, Atomic layer deposition of lead sulfide thin films for quantum confinement, *Chem. Mater.*, 2009, **21**, 3973–3978.

84 R. Kumar, R. Das, M. Gupta and V. Ganesan, Preparation of nanocrystalline Sb doped PbS thin films and their structural, optical, and electrical characterization, *Superlattices Microstruct.*, 2014, **75**, 601–612.

85 A. Mosbah and M. Aida, Influence of deposition temperature on structural, optical and electrical properties of sputtered Al doped ZnO thin films, *J. Alloys Compd.*, 2012, **515**, 149–153.

86 J. M. Pawlikowski, J. Misiewicz and N. Mirowska, Direct and indirect optical transitions in Zn_3P_2, *J. Phys. Chem. Solids*, 1979, **40**, 1027–1033.

87 A. Ekinci, Ö. Şahin and S. Horoz, Chemical bath deposition of Co doped PbS thin films for solar cell application, *J. Mater. Sci.: Mater. Electron.*, 2020, **31**, 1210–1215.

88 M. H. Jameel, S. Saleem, M. Hashim, M. S. Roslan, H. H. N. Somaily, M. M. Hessin, Z. M. El-Bahy, M. G. B. Ashiq, M. Q. Hamzah and A. H. Jabbar, A comparative study on characterizations and synthesis of pure lead sulfide (PbS) and Ag-doped PbS for photovoltaic applications, *Nanotechnol. Rev.*, 2021, **10**, 1484–1492.

89 E. Yücel and Y. Yücel, Fabrication and characterization of Sr-doped PbS thin films grown by CBD, *Ceram. Int.*, 2017, **43**, 407–413.

90 X. Zheng, F. Gao, F. Ji, H. Wu, J. Zhang, X. Hu and Y. Xiang, Cu-doped PbS thin films with low resistivity prepared via chemical bath deposition, *Mater. Lett.*, 2016, **167**, 128–130.

91 J. Huo, W. Li and T. Wang, Effect of Cr doping concentration on the structural, optical, and electrical properties of lead sulfide (PbS) nanofilms, *Coatings*, 2019, **9**, 376.

92 A. M. Ahmed and M. Rabia, Mohamed Shaban, The structure and photoelectrochemical activity of Cr-doped PbS thin films grown by chemical bath deposition, *RSC Adv.*, 2020, **10**, 14458–14470.

93 A. Javed and J.-B. Sun, An investigation of structural phase transformation and electrical resistivity in Ta films, *Appl. Surf. Sci.*, 2010, **257**, 1211–1215.